POLITECNICO
MILANO 1863

A New Storable Liquid Propulsion Family

Grattagliano Paola	10622298
Ippolito Annachiara	10661425
Malandra Andrea	10664092
Mantuano Luca	10664692
Martire Davide	10606727
Paris Sergio	10578218
Pilo Elena	10761604

Acronyms

Symbols

A_c Combustion chamber area.
A_e Exit area.
A_t Throat area.
A_{inj} Injector area.
B Blow-down ratio.
C_d Discharge coefficient.
C_t Thrust coefficient.
D_f Darcy friction factor.
FU Fuel subscript.
I_{sp} Specific impulse.
L^* Characteristic length.
L_{pipes} Pipes length.
M Mass.
M_m Molar mass.
OF Mixture ratio.
OX Oxidiser subscript.
P_c Chamber pressure.
P_{tank} Tank pressure.
R Perfect gas constant.
Re Reynold's number.
T Temperature.
T_c Chamber temperature.
T_f Final temperature.
T_i Initial temperature.
T_{lim} Thrust limit.
T_{nom} Nominal thrust.

V Volume.
ΔP_{check} Check valve pressure drop.
ΔP_{latch} Latch valve pressure drop.
ΔP_{pinch} Additional concentrated pinch pressure drop.
α Divergence angle.
$\dot{m}$ Mass flux.
γ Specif heat ratio.
μ Viscosity.
ρ Density.
θ_e Rao final parabola angle.
θ_i Rao initial parabola angle.
ε Expansion ratio.
c^* Characteristic velocity.
d Diameter.
d_{pipes} Pipes diameter.
dt Time step.
r_e Exit radius.
r_t Throat radius.
t_{burn} Burning time.
v_{pipes} Velocity in the pipes.

I

IN718 Inconel 718.

S

SLM Selective Laser Melting.

Contents

List of Figures

List of Tables

1 Introduction

1.1 Scope of the report and requirements

The MICIOBAU Propulsion Company is planning a new liquid propulsion system providing 100 N thrust, planning an extension to 10 N and 1000 N.
The engine to be designed is a liquid bipropellant running the couple H_2O_2 (87.5%) and RP-1, fitted with regenerative cooling. The feeding system relies on a blow-down architecture characterized by only two tanks. Each tank contains both the pressurizer gas and the fuel (or oxidizer) separated by an elastic bladder. Feeding lines and tanks are made up of stainless steel AISI 316, whereas the combustion chamber is produced through additive manufacturing with Inconel 718.
The purposes of the report are to:

- Summarize the design work-flow of the 100 N unit. (including nozzle, tanks, injection plate);

- Characterize the propulsion parameters (specific impulse and thrust) during the firing, as a function of time;

- Identify and include in the design the non-negligible sources of uncertainties for the nominal thrust (related to machinability, accuracy, production capability, etc...);

- Perform a statistical analysis to assess the uncertainties effects on the nominal performance, in particular the thrust and specific impulse, and qualitatively extend this analysis to the other systems of the family.

1.2 Propellant couple: H_2O_2 and RP-1

The use of hydrogen peroxide as an oxidizer in bi-propellant liquid rocket engines has undergone a renewed interest thanks to its benefits, especially for its non-toxicity, high density and low cost [6]. However, for the purpose of the design here reported, the following aspects must be stressed:

- H_2O_2 can be used in different concentrations. However, for the following design it was required to consider a percentage in mass of 87.5 of hydrogen peroxide, so all data are retrieved for this specific composition;

- H_2O_2 based engines usually exploit a catalytic bed to initially decompose the peroxide. Since in the design the catalytic bed sizing is not considered, the combustion chamber length will be higher to cope with with the higher residence time needed to account for the evaporation of the peroxide;

- Although the design of the cooling system was not requested, the rough computation about the length of the pipes was made by assuming that RP-1 is used as a coolant. Indeed, hydrogen peroxide decompose exothermically at low temperature[16] so it would trigger an explosive reaction across cooling pipes.

1.3 Metal additive layer manufacturing

One of the requirements set by the company is to build the combustion chamber in Inconel 718 with additive layer manufacturing.
Inconel 718 (IN718) [7] is a Ni-Cr based super alloy used in high temperature applications, renowned for its thermal and strength properties under extreme temperatures and mechanical conditions, especially

useful in fields such as the aviation and space ones.

Additive manufacturing has become more and more appealing to space industry, since it allows to achieve high performance and reliability, to reduce the weight of components, lead time and associated costs and the ability to design and manufacture complex geometries. It is also possible to manufacture, all at once, larger and more complex components, avoiding junctions between elements, therefore reducing costs of production and risks of potential failure modes across joints. [5] Moreover, post machining processes could be avoided since this technology enables near-final-shape products that needs only minor surface refinements.

Several companies employed IN718 for combustion chambers and injector plates, such as ArianeGroup [2]. Setting as objective 40–50% lower production costs for the Ariane 5, additive manufacturing allowed to have increased cost efficiency and performance. The injector core, in Figure 1.1, was indeed produced on an EOS M 400–4 system utilizing 4-laser technology thanks to which a decreased production time was possible.

Figure 1.1: ArianeGroup AM injector head [2]

Many papers report that IN718 is best treated with a powder bed fusion technology, more precisely with Selective Laser Melting (SLM), therefore the design employed data referred to this type of process and to this particular alloy. Moreover, SLM is characterised by high dimensional accuracy and excellent mechanical properties; on the other end, the process could take plenty of time and the chamber size of SLM machine limits the size of the parts that can be produced.

The more suitable way of manufacturing the propulsion unit is to start from the injection plate and proceed to the nozzle. Thus reducing the number of structures to support the motor during the production, which would lead to worsen surface accuracy once removed. Moreover, placing supporting structures is not always feasible, since these require to be compliant with the size and shape of the motor.

In order to build liquid rocket motors such as the one commissioned by the company, it is necessary to consider production uncertainties due to the machinery chosen.
In Appendix A, some of the most significant uncertainties [8] are reported, which are then used to perform the computations that can be found starting from the next section.

2 Nominal Design

This chapter focuses on the nominal design of the engine. In each section, a phase of the design is explained.

2.1 Input data

In order to start with the computation of the design of the requested engine, the following specifications must be taken into account:

P_c	T_{nom}	t_{burn}	ε	T_{lim}
20 bar	100 N	100 s	80	50 N

Table 2.1: Input data

The engine shall be designed such that the thrust at $t_{burn} = 100\,s$ is at least T_{lim}.

Data on H_2O_2 [16] and RP-1 [14] are reported in Table 2.2.
Hydrogen Peroxide is in High Test Peroxide configuration, thus the oxidizer density needs to be computed such that 87.5% in mass is made of H_2O_2 while the remaining part is water. Therefore, the oxidizer density is $\rho_{OX} = 1.37 \cdot 10^3 \frac{kg}{m^3}$

	Pure H_2O_2	RP-1
$\rho\ [\frac{kg}{m^3}]$	1450	807
$\mu\ [Pa \cdot s]$	$1.26 \cdot 10^{-3}$	$0.75 \cdot 10^{-3}$

Table 2.2: Properties of H_2O_2 and RP-1

2.2 CEA analysis

P_c [bar]	20
ε [-]	80
OF [-]	6.5
T_{FU} [K]	298
T_{OX} [K]	298

Table 2.3: CEA input

To get the thermodynamic parameters to use for the chamber design, the frozen problem in NASA CEA is solved by giving the data summarized in Table 2.3 as input.
Actually, RP-1 enters in the combustion chamber at a higher temperature than the ambient one, due to the heat exchanged with the thrust chamber from the regenerative cooling. However, NASA CEA's thermodynamic library only includes RP-1 at $T = 298\ K$, so a strong assumption on the RP-1 input temperature was made in order to get the values from CEA for the design. This leads to an engine design with slightly worse performances than reality, since RP-1 directly injected at lower temperature requires more enthalpy from the combustion chamber to heat up and burn.

During the firing, CEA input parameters will vary. In order to account for that, results of CEA are interpolated for multiple values of OF, T_c and P_c. The obtained graph can be found in Appendix B in Figure B.2.
From the CEA values, the characteristic velocity is found using D.2. Its value is $c^* = 1572.1\ m/s$.

2.3   Thrust chamber design

The thrust chamber sizing starts from the nozzle design. The expansion ratio is imposed. The exit pressure is found using an iterative process using the eq. (D.1) and, by passing through the computations of performances parameters such as characteristic velocity, thrust coefficient and exit velocity, the following sizing is obtained:

A_t [mm^2]	r_t [mm]	A_e [mm^2]	r_e [mm]	$\dot{m}$ [$\frac{kg}{s}$]	$\dot{m}_{fuel}$ [$\frac{kg}{s}$]	$\dot{m}_{ox}$ [$\frac{kg}{s}$]
25.51	2.85	20.4	25.5	0.0325	0.0043	0.0282

Table 2.4: Sizing results of combustion chamber

The nozzle is designed using the Rao approximation. Thus, a conical nozzle with divergence angle $\alpha = 15°$ is considered. The objective is to maximize the performance of the engine, hence, 100% of the length of the divergent part of the conical nozzle is chosen. Moreover, a bigger final angle would increase the difficulties in the additive manufacturing production process, which would lead to higher uncertainties in θ_e values.

The initial parabola angle is $\theta_i = 30.5893°$, while the final parabola angle is $\theta_e = 4.4464°$. The thrust is $T = 99.35$ N. This gives the nozzle an efficiency ratio of 99.35% with respect to the nominal $1D$ value of $T_{nom} = 100$ N. From approximated calculations of the modified Reynolds number, a value in the order of 10^8 is found. By comparing it with graphical data, available in Figure C.2 in Appendix C, the contribution due to the displacement thickness is negligible. Still, a more refined analysis shall be carried out to confirm this rough analysis. Table 2.5 summarizes the performance parameters of the engine.

Figure 2.1: $L_{Rao} = 100\%$ L_{ref}

The combustion chamber is designed starting from its section area A_c. The computation has been made considering a chamber mach number equal to 0.1. This value was selected to comply with the higher boundary of 0.3 to avoid compressibility of the fluid and to get a reasonable thrust chamber length to chamber area ratio. Results of these choices lead to a $A_c = 152$ mm^2. The contraction ratio for the designed engine equals to 5.96, which is higher than 3. Therefore, losses in the combustion chamber are negligible.

T_{rao} [N]	I_{sp} [s]	C_T [-]
99.35	311.84	1.9579

Table 2.5: Performance results

The next step of the design is the characterization of the length of the combustion chamber. To do that, an L^* must be chosen.

After an extensive literature research, no characteristic lengths for the selected design were found. The propellant couple is not yet a common configuration of neither tested engines nor experimental ones. Moreover, hydrogen peroxide is almost solely utilized with the application of a catalyst bed to help its decomposition process. A range of L^* between 1.524 and 1.778 were found in literature [9], considering the presence of a catalytic bed. Its absence will lower the chemical kinetics of the propellant combustion, thus an higher L^* is to be expected.

As a result of the just mentioned considerations, $L^* = 2$ is selected. This is an arbitrary value which is not supported by existing tests. An extensive testing campaign should be carried out in order to be able to choose a value with better observation.

The volume and length are then computed. The thrust chamber is thus fully characterized.

2.4   Feed line and valves

The feed line enables the flow of the propellants from the tanks to the combustion chamber. Each feed line is composed by AISI 316 1/8" pipes, a latch valve and a check valve. The system uses the Vacco V1E10454-01 [17] as latch valve and the Swagelok C Series [15] as check valve. They are both flight

qualified.

AISI 316 has a rather low roughness of around $0.8\mu m$, which keeps head losses of the pipe line relatively low. The latch valve is solenoid activated and gives the possibility to stop the flow. The check valve, instead, is a safety measure that allows the flow only in one direction. The H_2O_2 feed line directly goes from the tank to the injection plate, having a total length of 40 cm. On the other side, the RP-1 line is used for the regenerative cooling of the thrust chamber, thus the pipe line has a longer length, equalling to 1.17 m. Those lengths are selected by taking into account the size of the valves, the needed length for the fuel line for the regenerative cooling, and margins to keep the tanks at a safety distance from the thrust chamber. The D_f used for the calculations of the pipe head losses follows two different laws (see figure C.4) depending on the Reyonolds number computed. This leads to a discontinuity in the results during the firing, as it will be later explained in section 3.2.

An additional pressure drop of 5 bar is intentionally introduced in order to guarantee an adequate pressure difference between the tanks and the combustion chamber. This is usually done to avoid pressure fluctuations and mass flow rate instability. The concentrated pressure drop is achieved by introducing a restriction with diameter $d = 1\,mm$ into the feeding line [14].

2.5 Propellant tanks

In nominal conditions, the propellant tanks shall guarantee a combustion chamber pressure of 20 bar, taking into account the losses caused by pipes, valves and the injector. Since the system operates in blow-down mode, the pressure decreases during the firing. Therefore, the sizing is done on the initial pressure, which is the maximum one. The material used for the tanks is AISI 316. Being a chromium-molibdenum steel alloy, among other metals it has a relatively high heat capacity and more importantly a thermal conductivity equal to 18 $\frac{W}{m^2K}$. Since this value is quite low the expansion can be considered as adiabatic.

The selected pressurizing gas is N_2, having the following characteristics:

- Specific heat ratio: $\gamma = 1.4$

- Molar mass: $M_m = 28.02 \cdot 10^{-3} \frac{kg}{mol}$

Starting from the nominal mass flow rate and the burning time, it is possible to retrieve the mass of fuel and oxidizer needed. According to ESA margins [1], a 10% is added to the total propellant mass. A 2% is also added to the volume to take into account the density changes.

The pressure losses across the line are the followings:

1. Increment of dynamic pressure at tank exit;
2. Losses across the feeding line;
3. Pressure drop caused by the valves;
4. Additional pressure drop of 5 bar.

At this point, all initial conditions are fixed:

	H_2O_2 Tank	RP-1 Tank
T_i [K]	298	298
$P_{N_{2_i}}$ [bar]	29.2	25.6
V_p [m^3]	$2.30 \cdot 10^{-3}$	$6.02 \cdot 10^{-4}$

Table 2.6: Tanks initial conditions

The final temperature is imposed and equalized to 260 K, which is a suitable value to avoid H_2O_2 freezing T (255 K) and to guarantee a smooth variation of mass flow rate during firing. Using the equation for the adiabatic expansion D.3, it is possible to retrieve the final pressure at the end of the firing and then the volume and mass of tanks as well as that of the pressurizing gas. The obtained results are here reported:

5

	H_2O_2 Tank	RP-1 Tank
T_f [K]	260	260
$P_{N_{2_f}}$ [bar]	18.1	16.3
V_{tot} [m^3]	$5.02 \cdot 10^{-3}$	$1.37 \cdot 10^{-3}$
$V_{N_{2_i}}$ [m^3]	$2.72 \cdot 10^{-3}$	$7.67 \cdot 10^{-4}$
M_{N_2} [kg]	$2.5 \cdot 10^{-3}$	$6.1 \cdot 10^{-4}$
B [-]	1.62	1.57

Table 2.7: Tanks final conditions

In order to maximize the volume to surface ratio and to facilitate the placement of the bladder, a spherical shape for the tanks is selected. Naturally the choice of the shape shall take into account different system requirements, which are not considered in this design. Starting from the yield strength of the AISI 316 (290 MPa) and setting a burst pressure equal to twice the initial pressure of the pressurizing gas, it is possible to retrieve the minimum thickness needed for the tanks. The obtained value are 0.7 mm and 1 mm respectively for the fuel and the oxidizer tank. Therefore the tanks are capable to substain the define burst pressure.

2.6   Injector

Concerning the design of the injector plate, two different configurations are considered to guarantee an adequate mixing and atomization, taking also into account the machinability with SLM:

- **Coaxial swirl**: this kind of injectors has high mixing capacity and is used also for liquid-liquid injection. These injectors show smaller mean droplet diameter with respect to impinging injectors for the same mass flow rate. [10] [11]

- **Unlike**: These injectors are easier to be manufactured and have higher discharge coefficients.

The swirl coaxial injectors are nevertheless more prone to instability and have smaller discharge coefficients for the same orifice size. Due to the small diameter of the injection plate, the orifices size would have been too large to guarantee an adequate exit velocity, hence an unlike injector is selected for this application.

The chosen type of orifice is here reported: the diameter is equal to 1 mm, which is small enough to provide a good atomization, staying within the limits of the additive manufacturing process (see Appendix A).
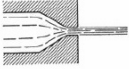
Orifice Type	Diagram	Diameter (mm)	Discharge Coefficient
Short tube with conical entrance		0.50	0.7
		1.00	0.82
		1.57	0.76
		2.54	0.84–0.80
		3.18	0.84–0.78

Figure 2.2: Discharge coefficient [14]

Once the type of injector is selected, it is possible to compute the overall area needed for the nominal mass flow rate. At least two orifices for the oxidizer and one for the fuel are necessary to cover the overall area, thus a triplet configuration is selected.

The real pressure drop across the orifices is then computed, resulting in an exit velocity equal to 7.38 $\frac{m}{s}$ for the fuel and 13.01 $\frac{m}{s}$ for the oxidizer. To fully characterize the geometry of the injector, the angle between the axis of the oxidizer hole and the normal to the injection plate is set equal to 30° [3]. Moreover, considering the angle of the holes flaring approximately equal to 20° and that the impinging occurs at 5 mm ca. from the injection plate, it is necessary to have an injector plate width of at least 3 mm.

3 Firing Simulation

Once the nominal design is completed, the performance of the propulsion unit over the nominal firing time is estimated with a simple algorithm. The aim is to ensure that the requirement on the thrust is satisfied over the whole firing, as well as to monitor the merit parameters of the engine.

3.1 Implementation

The algorithm implemented consists in a fixed step discretization in time of the problem. The starting values are set equal to the nominal design, then for each time step:

1. The oxidizer to fuel ratio OF and the combustion chamber pressure P_c are assumed to be equal to the previous step, and are used to compute the thermodynamics parameters T_c, γ, R by interpolation with data from NASA CEA;

2. P_c, $\dot{m}_{ox}$, $\dot{m}_f$ for the current iteration are computed by solving a system of 3 equation, nominally the two lines pressure drops equations and the c^* equation, which is assumed equal to the previous time step (see equation D.4 in appendix D);

3. The performance parameters are then computed from the knowledge of P_c, T_c, γ, R and $\dot{m}$ of the current time step.

By setting the dt to a reasonably low value, the result should approximately resemble the actual behaviour of the engine.

3.2 Results

The firing algorithm is run for different nominal starting OF, with dt set to 0.1 s, to identify the best performance in terms of thrust and specific impulse. In every case considered, the thrust never drops below the minimum value of $T_{lim} = 50\,N$ and the variability of both the thrust and combustion chamber pressure is very low, as shown in appendix F. The comparison between different OF also highlights the presence of discontinuities into the evolution of both the OF and I_{sp}. This is due to the fact that the
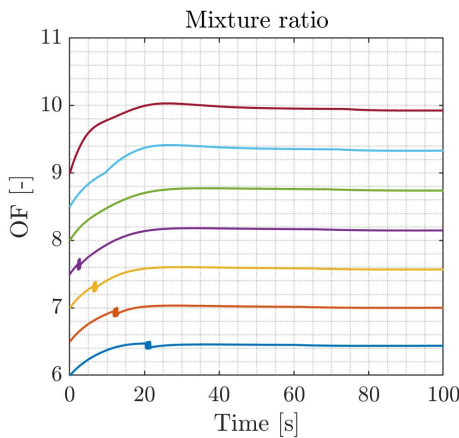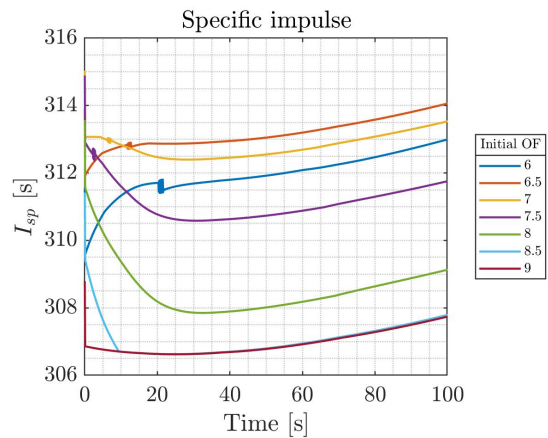

Figure 3.1: Thrust evolution

Figure 3.2: Specific impulse evolution

7

Darcy's friction factor D_f is modeled as $\frac{64}{Re}$ for Re less than 2000, and evaluated through interpolation of experimental data for Re higher than 2000. As seen from the Figure 3.2, the best performances in terms of I_{sp} are given by a nominal starting OF of 6.5. This is due to the fact that the evolution of OF stabilizes around a value close to the stoichiometric ratio of the couple (around 7).

The following analysis focuses on the performance evolution using the value of OF= 6.5 as the nominal starting one.
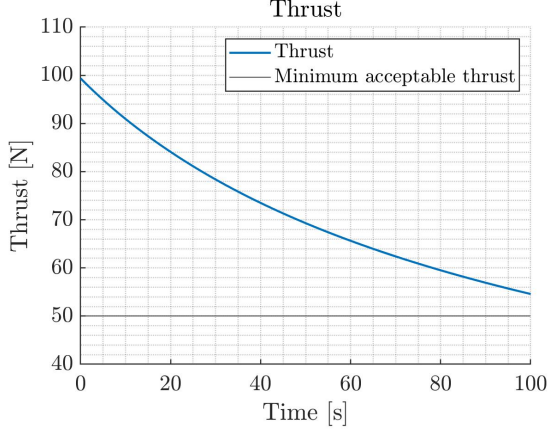
Figure 3.3: Thrust evolution
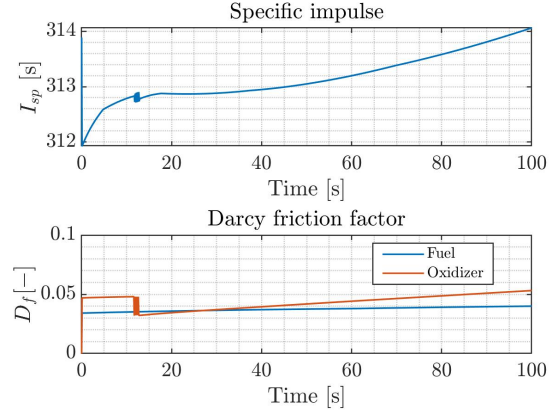
Figure 3.4: Specific impulse and D_f discontinuity

The thrust and I_{sp} evolution are shown in Figures 3.3 and 3.4 with a focus on the discontinuity problem due to the calculation of D_f.

Tanks pressure during firing and mass flow rate are plotted in figures 3.5 and 3.6 to explain the variability of both the thrust and combustion chamber pressure. The evolution of these three quantities is consistent with the expected behaviour and further confirm the validity of the model implemented.
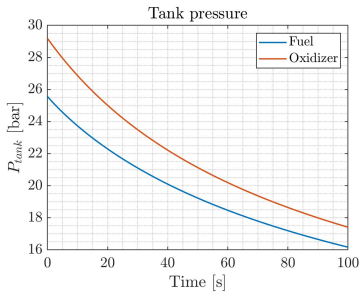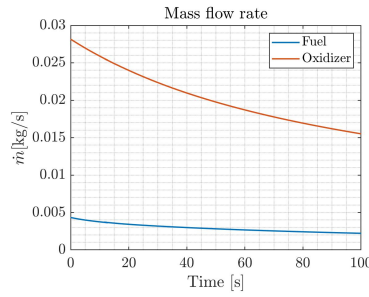

Figure 3.5: Tanks pressure evolution
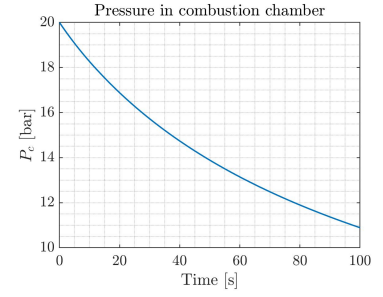

Figure 3.6: Mass flow rates evolution

Figure 3.7: Combustion chamber pressure evolution

4 Montecarlo Analysis

A Montecarlo statistical analysis is required to predict how the nominal design is affected by the uncertainties related to the production process of the engine. As a consequence, the propagation of those uncertainties will invalidate the nominal performances, evaluated in terms of both thrust and specific impulse.

4.1 Uncertainty sources: additive manufacturing

As stated before, the SLM technology was considered as a proper candidate for the production of the engine's thrust chamber. The process has an high accuracy also handling with complex internal and external features, but to be successfully applied to the system, the critical aspects in terms of geometry and reproducibility must be included.
The results deriving from the production of different geometries, and relative errors, are reported in Appendix A. For this particular engine, the following most critical aspects are highlighted to carry out the uncertainty analysis:

- **Hole reproducibility**: it affects the injection orifices accuracy since from the nominal design three injectors of equal area are identified. During production their relative size may slightly change;

- **Wall thickness**: it leads to uncertainties related to the engine structural behavior as well as variations of both internal and external geometries. This would also affect the regenerative cooling system (not analyzed in this study) giving uncertainties on the heat flux between the combustion chamber and the cooling channels;

- **Wall angles**: it affects the inclined geometries of the system, which include the oxidizer injectors and the nozzle (divergent and convergent part). The data found on this topic are related to inclined plane surfaces. For a more refined analysis model/experiments on conical/cylindrical geometries shall be taken into account, however the discrepancy should not be considerable.

- **Surface roughness**: it leads to small variations in the mass flow rate of the thrust chamber introducing small losses on the overall performances. For SLM, post-processing for the improvement of the surface roughness is usually not required due to high accuracy achieved with higher energy beams;

- **Vertical holes production**: these errors are related to the hole diameter;

Since the available computational capability was limited, only the most critical parameters were related to an uncertainty and fed to the nominal performances simulation. The mean values considered come from the nominal design, while the standard deviations were extrapolated from the literature [8] considering the various aspects previously exposed. All the values given as inputs for the analysis are reported in Table 4.1

Uncertainty	Mean Value	Standard Deviation	Relative
Throat area diameter	5.7 mm	10 μm	0.17 %
Nozzle exit angle	4.446°	0.025°	0.56 %
Fuel injector diameter	1 mm	10 μm	1 %
First oxidizer injector diameter	1 mm	10 μm	1 %
Second oxidizer injector diameter	1 mm	10 μm	1 %

Table 4.1: Uncertainties considered for the Montecarlo analysis

4.2   Method implementation

The Montecarlo analysis takes as inputs the mean values and standard deviations of all five uncertainties, as well as the population size N (50 due to computational limits).

Then it randomly generates N values for all constants, assuming a normal distribution due to their aleatory nature. Afterwards, it generates N^5 sets of five values and feeds them in a random order to the model. For each iteration, the values of thrust and specific impulse are saved and the cumulative mean value and standard deviation are computed.

Each $N/2$ iterations, the current values of mean and standard deviation are compared to the one of $N/2$ iterations before, and the relative error between the two steps is computed. If this error for both the quantities is less than a tolerance of $5 \cdot 10^{-4}$, a further control on the error is done with the previous iteration.

In the simulation implemented for the Montecarlo analysis, the thrust value is correlated to the uncertainties, fixing the geometry and the tanks pressure obtained from the nominal design:

$$T = T(d_{OX,1}, d_{OX,2}, d_{FU}, d_t, \theta_e)$$

In particular:

1. The uncertainties of the injection orifices and throat diameters fall into the system of equations D.5 (Appendix D), and propagates in the combustion chamber pressure and in the individual mass flow rates passing through the orifices. To close and solve the problem, it was decided to set constant the characteristic velocity as the nominal one ($c^* = 1572.06 \frac{m}{s}$), since this is an indicator of combustion efficiency and can be considered constant with a small error;

2. The new values of P_c and OF are introduced in the interpolation of CEA data, and as output a new value of γ is obtained;

3. The rest of the equations flow is identical to the nominal design, up to the RAO nozzle where the last source of uncertainty (the exit angle) is introduced and propagated in the 2D losses.

4. Finally the uncertainty on the thrust is propagated to the specific impulse, to evaluate the final effects on performances.

4.3   Results

Results of the Montecarlo analysis are obtained and presented in Table 4.2 and in Figures 4.1, 4.2,4.3, 4.4.

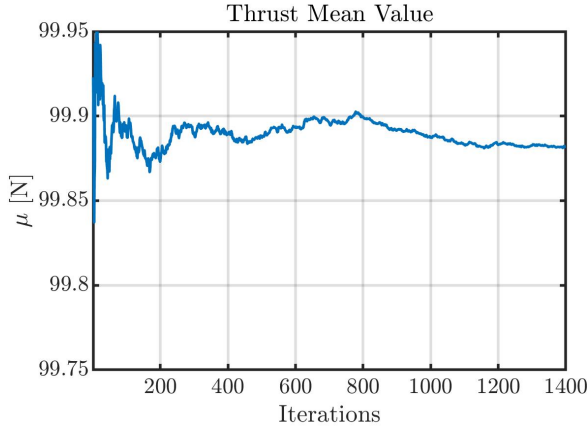| Performance	Mean Value	Standard Deviation	Relative
Thrust	99.882 N	0.303 N	0.303 %
Specific Impulse	313.229 s	0.043 s	0.013 %

Table 4.2: Montecarlo analysis results

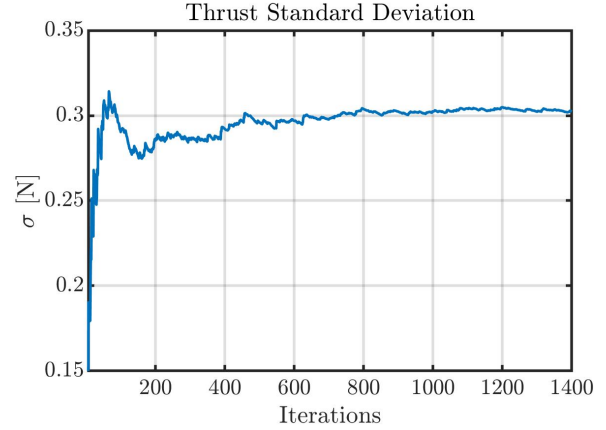Figure 4.1: Thrust mean value

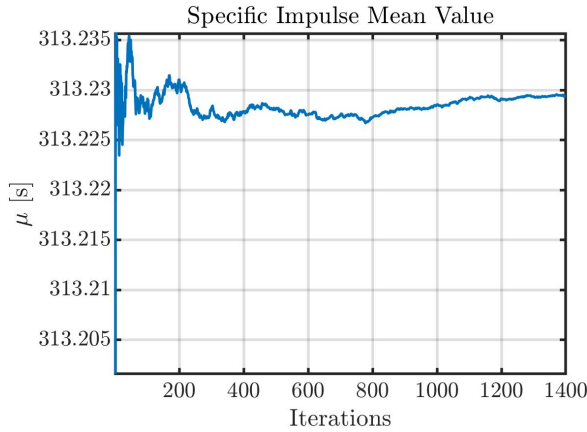Figure 4.2: Thrust standard deviation
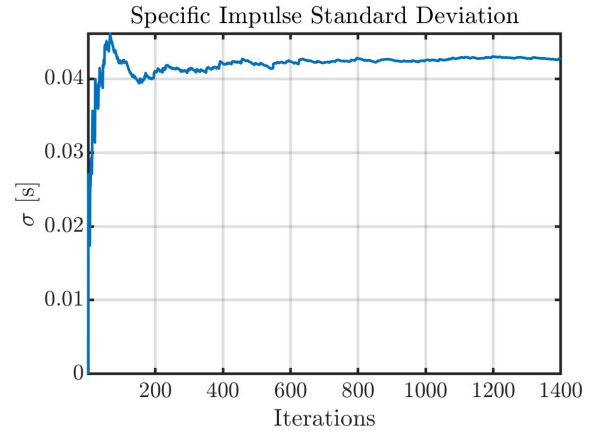

Figure 4.3: Specific impulse mean value

Figure 4.4: Specific impulse deviation

An observation must be done on the convergence behavior: it is affected by the limited population size, which could not be taken higher due to computational issues.

In the end, it can be shown how the relative uncertainties considered (Table 4.1) propagate when computing the uncertainties related to the performance parameters, as shown in Table 4.2. It seems that the relative uncertainty smooths out with respect to the starting uncertainties, and this is particularly evident in the case of the specific impulse.

As regard to the thrust, this is probably due to the fact that the most significant source of uncertainty is the throat area. The mass flow rate variations due to uncertainties on the injection orifices are negligible, because ΔP variation is really small with respect to the overall feed-line ΔP. Furthermore, the loss due to the nozzle's exit angle is a small variation of an angle into a cosine with argument smaller then 1 rad, therefore negligible too.

As for the specific impulse behaviour, the assumption of constant c^* may be the source of a such low uncertainty. Following the assumption of constant c^*, the C_t is negligibly influenced by the throat area uncertainty, because it is almost only affected in the static contribution part.

5   Conclusions

In conclusion, the requested design of the 100 N thruster is succesfully accomplished. In addition, the considerations on the production and machinability of the component seems reasonable and suitable for the application considered. The uncertainty analysis via Montecarlo gives a satisfactory understanding of the aleatory variables of the problem, mainly related to the production process.

In this framework, the design of the 100 N thruster is a first step to the production of a new storable liquid propulsion family. For this reason, to complete the discussion, a qualitative feasibility study over possible alternative versions of the engine is carried out, in particular by extending the nominal thrust to 10 N and 1000 N.

A 1000 N thruster design would result in a larger motor. Therefore, the additive manufacturing process would work on larger geometries resulting in smaller relative uncertainties both in terms of dimensions and surface finishing. For this reason, their propagation on the performances would be negligible leading to a more reliable engine.

On the other end, a 10 N thrust motor entails an increment in production uncertainties in absolute as well as in relative terms. Indeed, both laser beam and melting powder have a lower limit dimension, thus finer details are realized with worse surface finishing. Extremely critical would be the design of the injection plate, since the orifices' diameters would require to be reduced to a value that does not allow the employment of SLM. Indeed, it is usually advised not to design holes with a diameter of 0.5 mm or below to avoid the increasing possibility of occlusions due to fully melted material [13]. In addition, manufacturing such small propulsion systems would lead to a non negligible consideration of the roughness in both the combustion chamber and the nozzle, that would consequently influence the thrust.

Figure 5.1: Designed 100 N engine, schematic representation

Bibliography

[1] *ESA-TECSYE-RS-006510*, 2017.

[2] *EOS, Future Ariane propulsion module: Simplified by additive manufacturing, 2018*. ArianeGroup, 2018. URL `https://www.eos.info/01_parts-and-applications/case_studies_applications_parts/_case_studies_pdf/en_cases/cs_m_aerospace_arianegroup_en.pdf`.

[3] D. M. Atyam and P. E. Sojka. Characterization of direct metal laser sintered impinging injectors: Like-doublet, unlike triplet, unlike quadlet, unlike pentad. In *53rd AIAA/SAE/ASEE Joint Propulsion Conference*, page 4602, 2017.

[4] M. Balbaa, S. Mekhiel, M. Elbestawi, and J. McIsaac. On selective laser melting of inconel 718: Densification, surface roughness, and residual stresses. *Materials & Design*, 193:108818, 2020.

[5] B. Blakey-Milner, P. Gradl, G. Snedden, M. Brooks, J. Pitot, E. Lopez, M. Leary, F. Berto, and A. du Plessis. Metal additive manufacturing in aerospace: A review. *Materials & Design*, 209: 110008, 2021.

[6] M. S. R. BONDUGULA and S. GORAKULA. Hydrogen peroxide based green propellants for future space propulsion applications. 2021.

[7] M. Godec, S. Malej, D. Feizpour, Č. Donik, M. Balažic, D. Klobčar, L. Pambaguian, M. Conradi, and A. Kocijan. Hybrid additive manufacturing of inconel 718 for future space applications. *Materials Characterization*, 172:110842, 2021.

[8] P. R. Gradl, D. C. Tinker, J. Ivester, S. W. Skinner, T. Teasley, and J. L. Bili. Geometric feature reproducibility for laser powder bed fusion (l-pbf) additive manufacturing with inconel 718. *Additive Manufacturing*, 47:102305, 2021.

[9] G. Henry, R. Humble, W. Larson, U. S. D. of Defense, U. S. N. Aeronautics, and S. Administration. *Space Propulsion Analysis and Design*. College custom series. McGraw-Hill, 1995. ISBN 9780070313293.

[10] D. Morrow. *Minimizing hydraulic losses in additively-manufactured swirl coaxial rocket injectors via analysis-driven design methods*. University of California, Los Angeles, 2020.

[11] M. Popp, J. Hulka, V. Yang, and M. Habiballah. Liquid rocket thrust chambers: Aspects of modeling, analysis, and design, 2004.

[12] J. M. Seitzman. Losses and real nozzle effects. 2006.

[13] E. U. SOLAKOĞLU, R. YILMAZ, S. ÖREN, G. AKBULUT, Ö. POYRAZ, and E. YASA. Process limits of direct metal laser sintering (dmls) in terms of minimum hole and boss diameters with varying aspect ratios.

[14] G. Sutton and O. Biblarz. *Rocket Propulsion Elements*. Wiley, 2016. ISBN 9781118753651.

[15] *Check Valve Datasheet*. Swagelok. URL `https://www.swagelok.com/downloads/webcatalogs/en/ms-01-176.pdf`.

[16] *Hydrogen Peroxide Thermodynamic Properties*. USP Technologies, 2022. URL `https://www.h2o2.com/technical-library/physical-chemical-properties/thermodynamic-properties/default.aspx?pid=33&name=H2O2-Thermodynamic-Properties`.

[17] *Latch Valve Datasheet*. VACCO industries. URL `https://www.vacco.com/images/uploads/pdfs/latch_valves_low_pressure.pdf`.
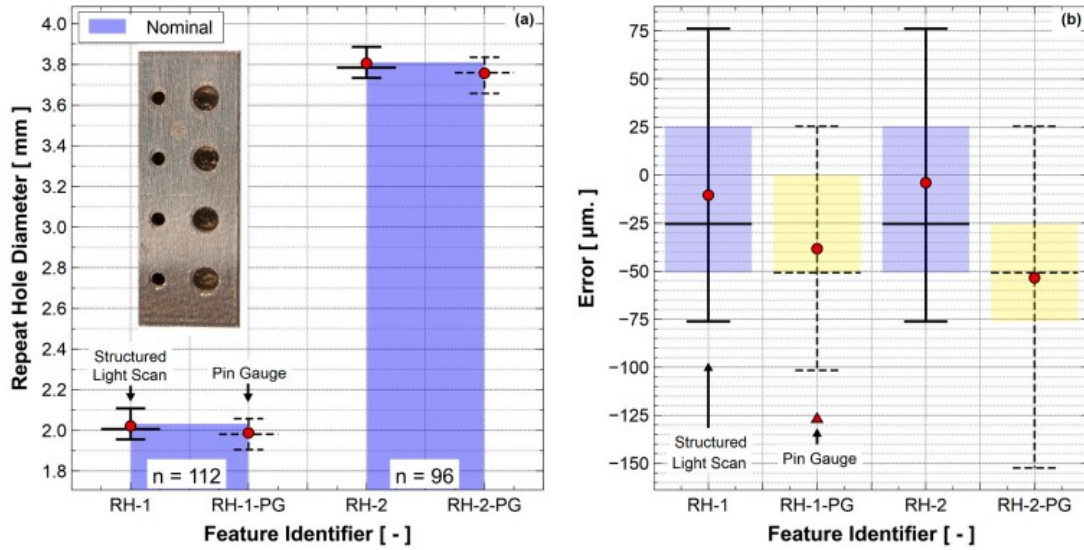
A   Additive manufacturing features

Figure A.1: Repeat Hole Variation with different machine configurations combined. (a) Overall Repeat Hole Diameters and (b) Deviation from repeat hole diameters [8]
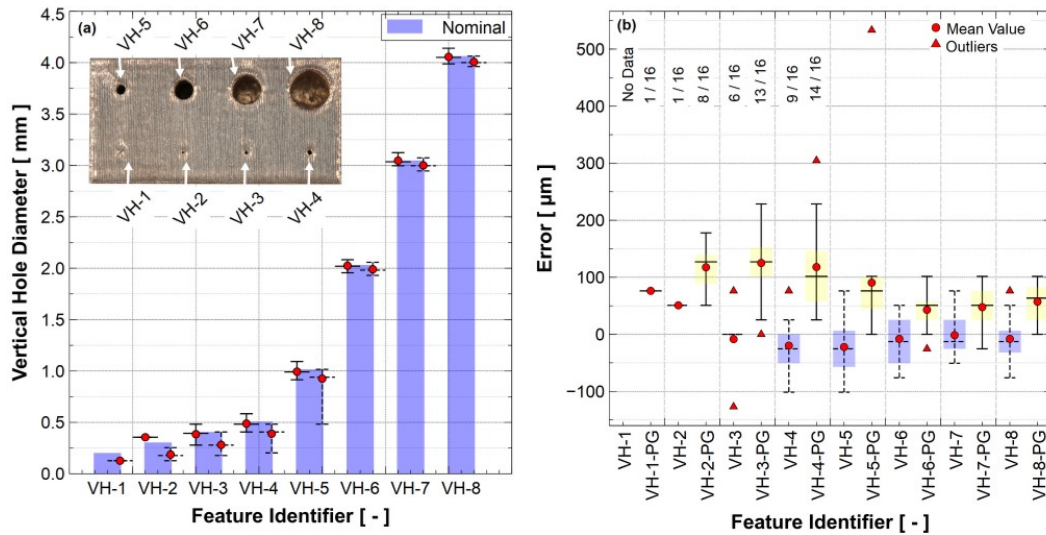

Figure A.2: Range of data from vertical holes compared with nominal values. Fractional values shown indicate incomplete data sets due to failed builds [8]
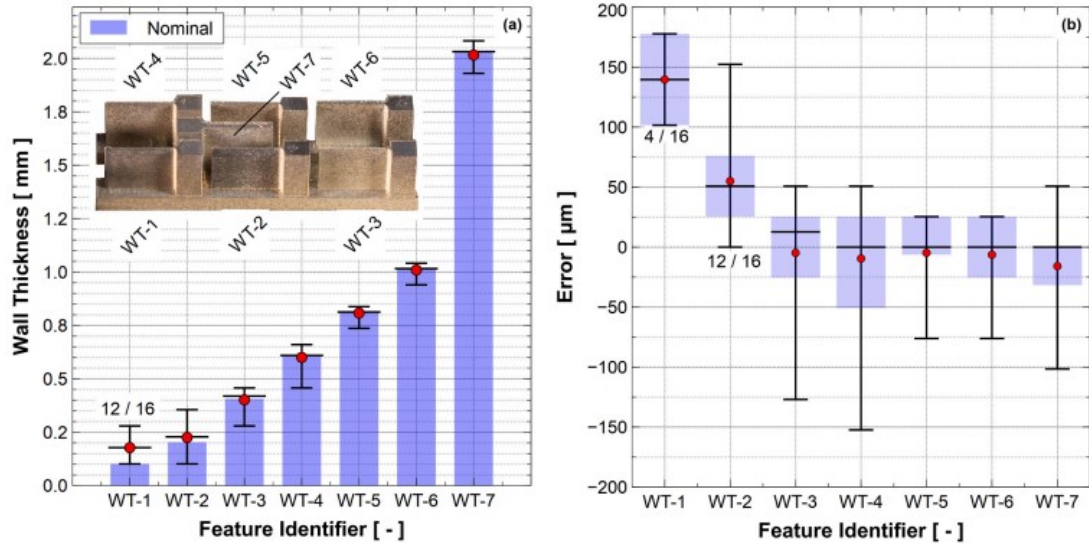
Figure A.3: Evaluation of wall thickness (a) Variation of wall thicknesses with nominal designed wall thicknesses. (b) Deviation of wall thickness from nominal with reduced data [8]
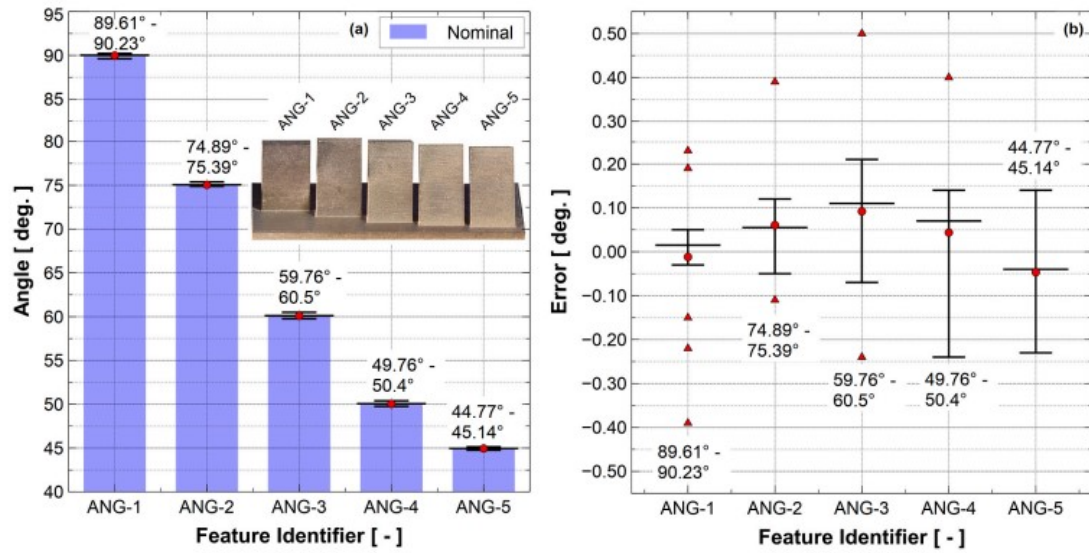
Figure A.4: Wall angles and wall angle deviation versus the angle identifier. Range maximum and minimums are displayed for each data set [8]
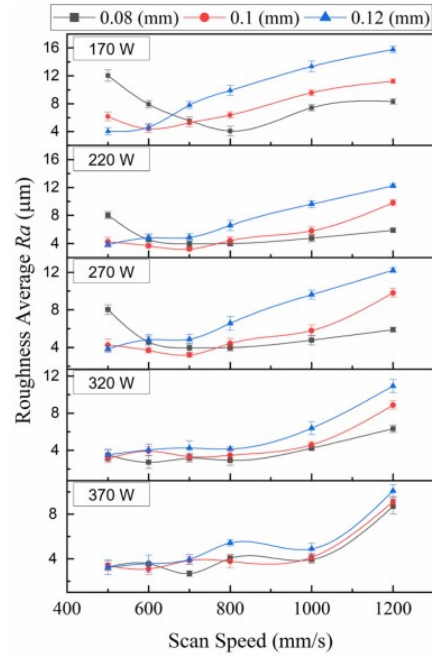
Figure A.5: Average surface roughness variation with process parameters [4]

B Thermochemical data
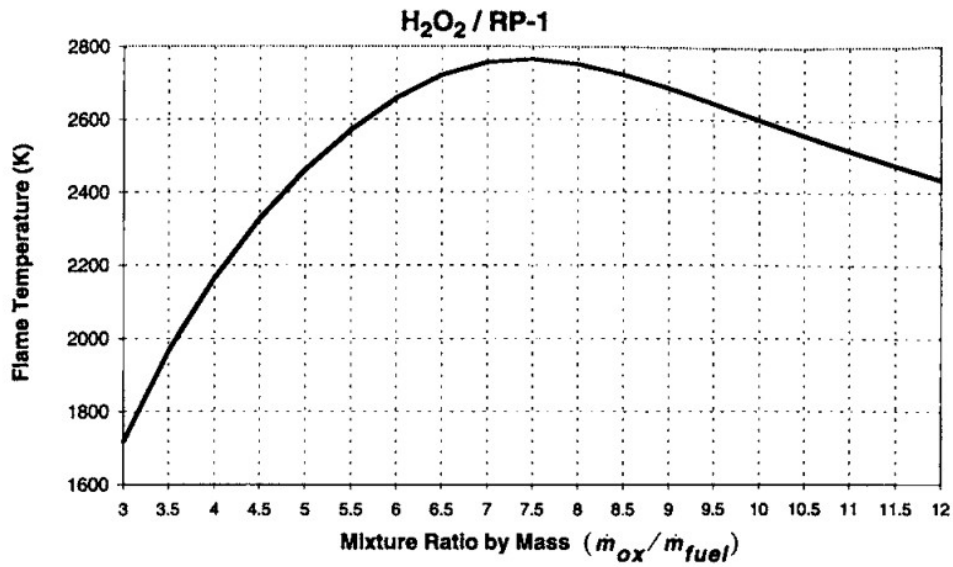
Figure B.1: Flame Temperature versus Mixture Ratio. The fuel is RP-1 and the oxidiser is 90% H_2O_2 by mass [9]
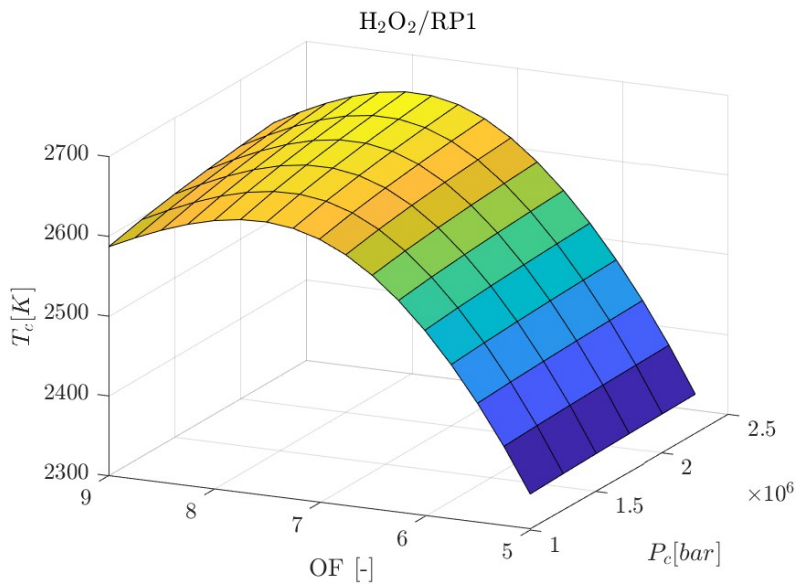
Figure B.2: Computed combustion chamber pressure (P_c) versus mixture ratio (OF) versus combustion chamber temperature (T_c). The fuel is RP-1 and the oxidiser is 87.5% H_2O_2 by mass

C   Engine design charts
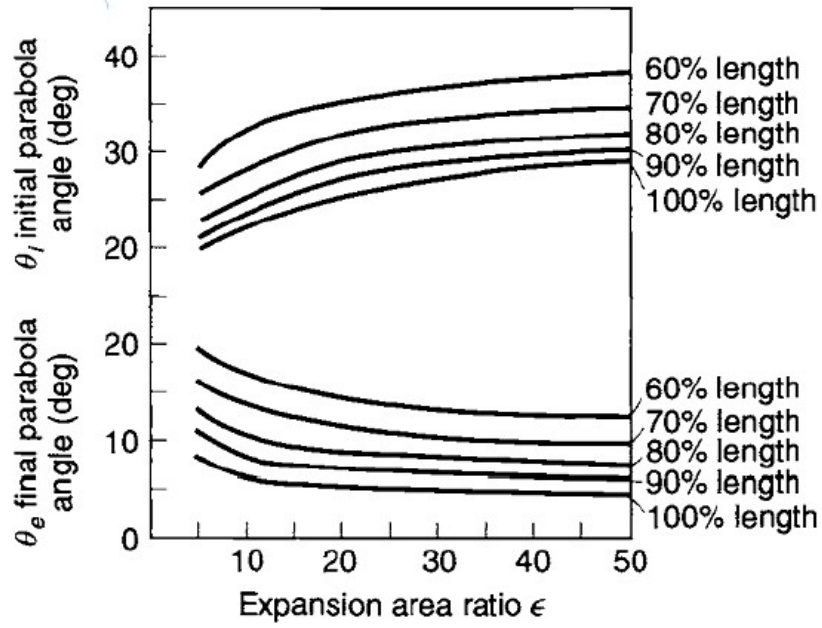
Figure C.1: Initial and final angle of the Rao approximation nozzle design [9]
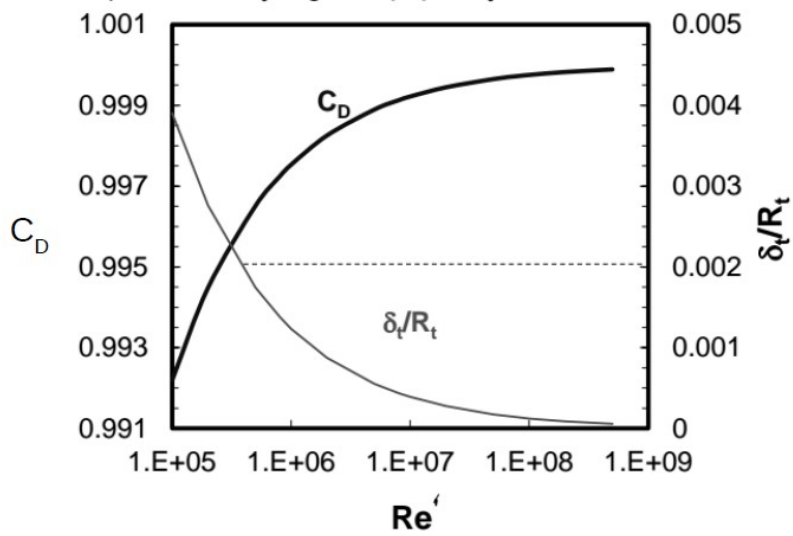
Figure C.2: Discharge coefficient evolution with respect to the modified Re for displacement thickness loss analysis [12]
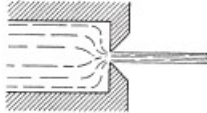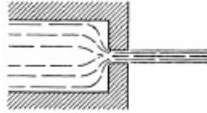
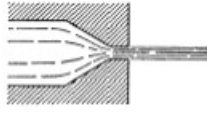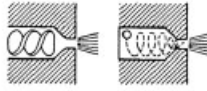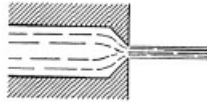| Orifice Type	Diagram	Diameter (mm)	Discharge Coefficient
Sharp-edged orifice		Above 2.5	0.61
		Below 2.5	0.65 approx.
Short-tube with rounded entrance $L/D > 3.0$		1.00	0.88
		1.57	0.90
		1.00	
		(with $L/D \sim 1.0$)	0.70
Short tube with conical entrance		0.50	0.7
		1.00	0.82
		1.57	0.76
		2.54	0.84−0.80
		3.18	0.84−0.78
Short tube with spiral effect		1.0−6.4	0.2−0.55
Sharp-edged cone		1.00	0.70−0.69
		1.57	0.72

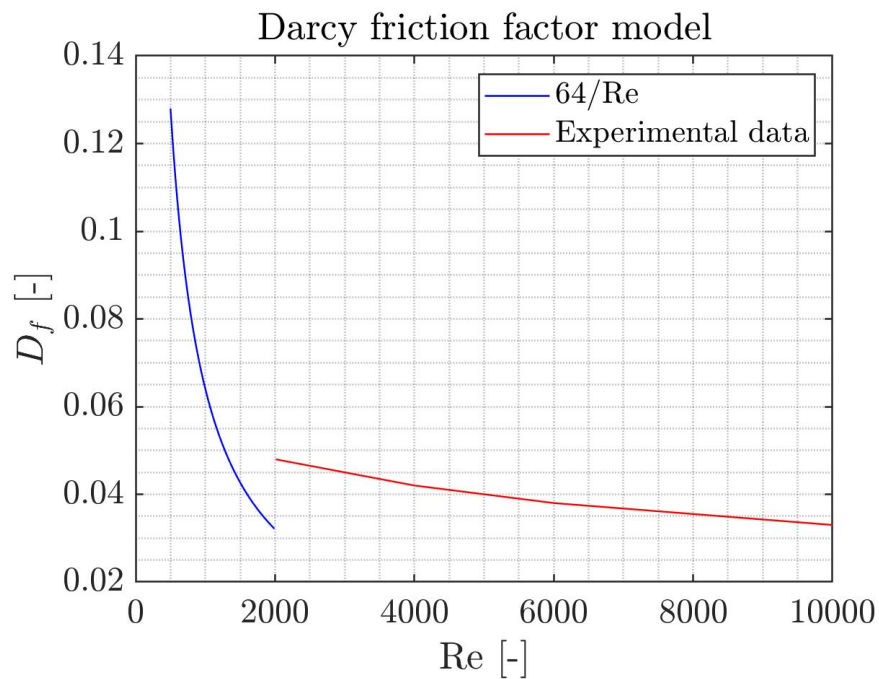Figure C.3: Discharge coefficient for different types of injector [14]

Figure C.4: Darcy friction factor model for relative roughness equal to $5.12 \cdot 10^{-4}$

D   Equations

$$\frac{1}{\varepsilon} = \left(\frac{\gamma+1}{\gamma}\right)^{\frac{1}{\gamma-1}} \left(\frac{P_e}{P_c}\right)^{\frac{1}{\gamma}} \sqrt{\frac{\gamma+1}{\gamma-1}\left[1-\left(\frac{P_e}{P_c}\right)^{\frac{\gamma-1}{\gamma}}\right]} \tag{D.1}$$

$$c^* = \frac{\sqrt{RT_c}}{\Gamma(\gamma)} \tag{D.2}$$

where:

$$\Gamma(\gamma) = \sqrt{\gamma\left(\frac{2}{\gamma+1}\right)^{\frac{\gamma+1}{\gamma-1}}}$$

$$\left(\frac{P_{fin}}{P_{in}}\right)^{\frac{k}{k-1}} = \frac{T_{fin}}{T_{in}} \tag{D.3}$$

$$\begin{cases} P_{tank,FU} - P_c - \dfrac{1}{2}\dfrac{L_{pipes}D_f}{d_{pipes}}\rho v^2_{pipes,FU} - \Delta P_{drop} - \dfrac{1}{2}\rho v^2_{pipes,FU} - \rho\left(\dfrac{\dot{m_{FU}}}{A_{inj,FU}C_d}\right)^2 = 0 \\[4mm] P_{tank,OX} - P_c - \dfrac{1}{2}\dfrac{L_{pipes}D_f}{d_{pipes}}\rho v^2_{pipes,OX} - \Delta P_{drop} - \dfrac{1}{2}\rho v^2_{pipes,OX} - \rho\left(\dfrac{\dot{m_{OX}}}{A_{inj,OX}C_d}\right)^2 = 0 \\[4mm] c^* - \dfrac{A_t P_c}{\dot{m_{OX}} + \dot{m_{FU}}} = 0 \end{cases} \tag{D.4}$$

$$\begin{cases} P_{tank,FU} - P_c - \dfrac{1}{2}\dfrac{L_{pipes}D_f}{d_{pipes}}\rho v^2_{pipes,FU} - \Delta P_{drop} - \dfrac{1}{2}\rho v^2_{pipes,FU} - \rho\left(\dfrac{\dot{m_{FU}}}{A_{inj,FU}C_d}\right)^2 = 0 \\[4mm] P_{tank,OX1} - P_c - \dfrac{1}{2}\dfrac{L_{pipes}D_f}{d_{pipes}}\rho v^2_{pipes,OX1} - \Delta P_{drop} - \dfrac{1}{2}\rho v^2_{pipes,OX1} - \rho\left(\dfrac{\dot{m_{OX1}}}{A_{inj,OX1}C_d}\right)^2 = 0 \\[4mm] P_{tank,OX2} - P_c - \dfrac{1}{2}\dfrac{L_{pipes}D_f}{d_{pipes}}\rho v^2_{pipes,OX2} - \Delta P_{drop} - \dfrac{1}{2}\rho v^2_{pipes,OX2} - \rho\left(\dfrac{\dot{m_{OX2}}}{A_{inj,OX2}C_d}\right)^2 = 0 \\[4mm] c^* - \dfrac{A_t P_c}{\dot{m_{OX1}} + \dot{m_{OX2}} + \dot{m_{FU}}} = 0 \end{cases} \tag{D.5}$$

where:

$$\Delta P_{drop} = \Delta P_{latch} + \Delta P_{pinch} + \Delta P_{check}$$

$$\dot{m} = C_d\, A_c\, \sqrt{2\,\Delta P\,\rho} \tag{D.6}$$

E   Valves features

Valves' pressure drop graphs are referred to water. To evaluate the pressure drop of the two propellants a ratio between the propellant density ad the water density is added into the equation.
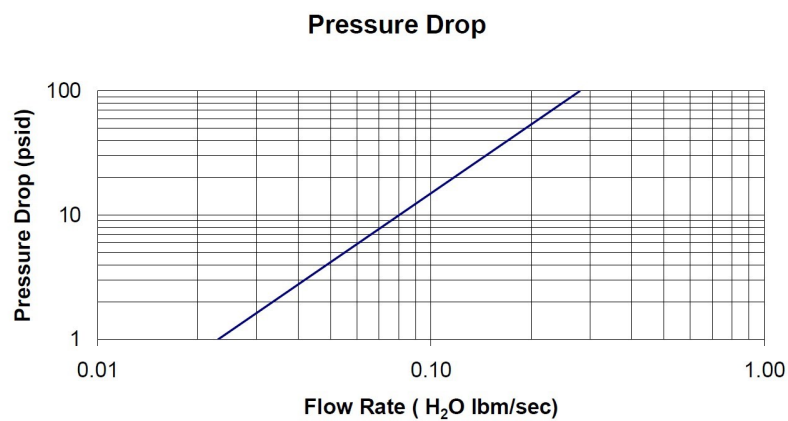

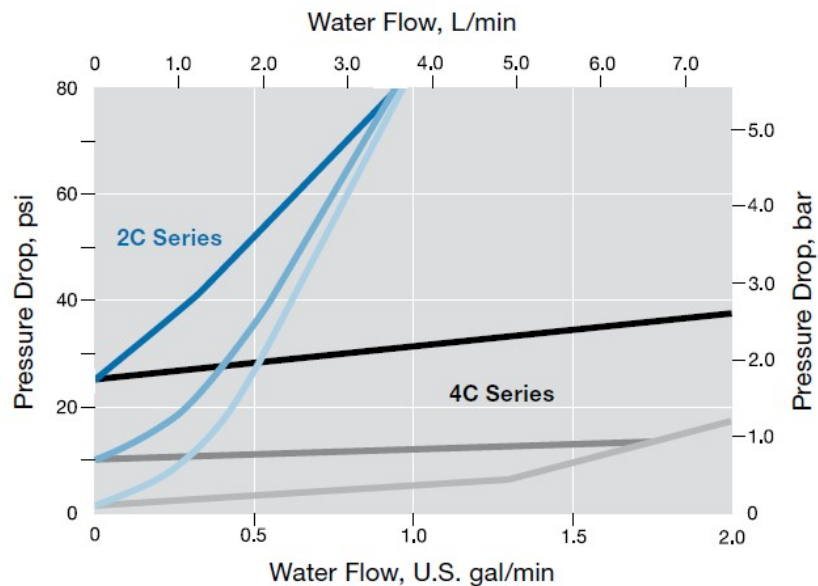Figure E.1: Vacco V1E10454-01 latch valve pressure drop

Figure E.2: Swagelok 2C series check valve pressure drop. The selected valve follows the lightest blue line, which allows a cracking pressure of 1 psi

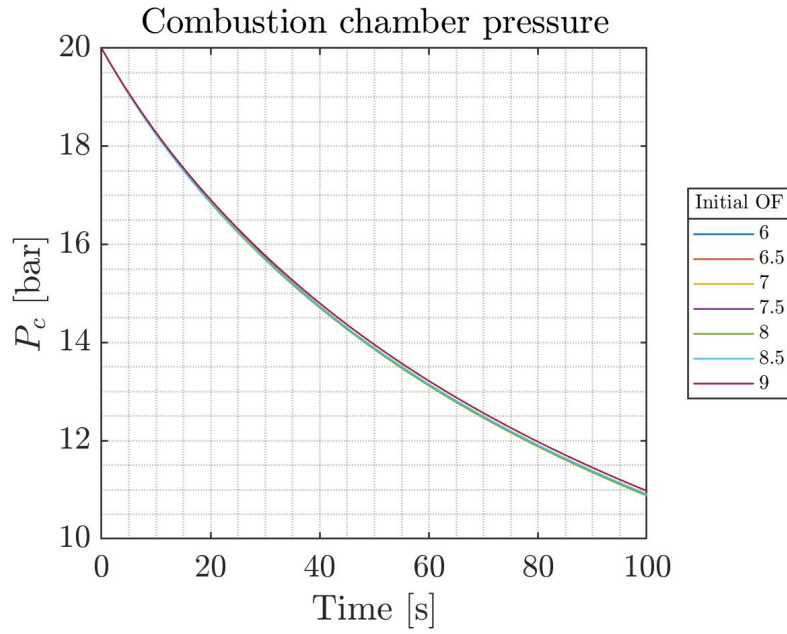# F   Properties as function of OF ratio
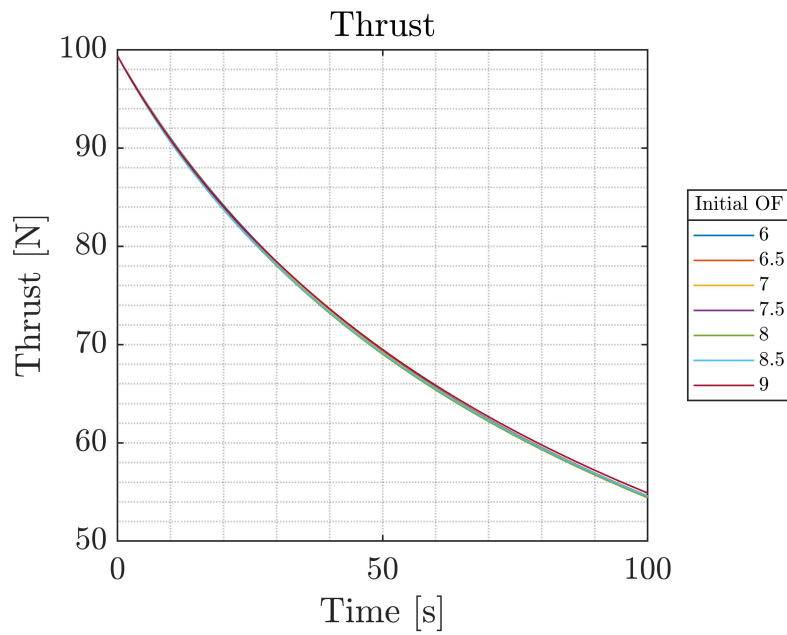

Figure F.1: Combustion chamber pressure as function of OF ratio

Figure F.2: Thrust as function of OF ratio